Applied Catalysis B: Environmental 165 (2015) 128–138

Contents lists available at ScienceDirect

Applied Catalysis B: Environmental

journal homepage: www.elsevier.com/locate/apcatb

Solution grown ZnO rods: Synthesis, characterization and defect mediated photocatalytic activity

Soumita Mukhopadhyay[a,b], Partha Pratim Das[a,b], Suvendu Maity[c], Prasanta Ghosh[c], P. Sujatha Devi[a,b,*]

[a] Nano-Structured Materials Division, CSIR-Central Glass and Ceramic Research Institute (CSIR-CGCRI), 196, Raja SC Mullick Road, Jadavpur, Kolkata 700 032, India
[b] CSIR-Network Institute of Solar Energy (CSIR-NISE), New Delhi, India
[c] Department of Chemistry, R. K. Mission Residential College, Narendrapur, Kolkata 700103, India

ARTICLE INFO

Article history:
Received 31 May 2014
Received in revised form
14 September 2014
Accepted 22 September 2014
Available online 28 October 2014

Keywords:
Solution growth
ZnO rods
Methyl violet
Shallow donor
Photodegradation

ABSTRACT

The aqueous solution growth process of ZnO rods, starting from zinc hydroxide formed during the ultrasonic precipitation of zinc acetate and ammonium hydroxide has been demonstrated here. A dispersion consisting of 0.3 (w/v) % zinc hydroxide in water on heating at 80 ± 5 °C for 6 h has resulted in the formation of ZnO rods having an aspect ratio between 8 and 12. We have monitored the growth of ZnO rods as a function of different reaction parameters. The as-prepared rods have also been characterized by optical and Raman spectroscopic methods in addition to other techniques. Further, we also investigated the photocatalytic degradation of methyl violet, which is a well known textile pollutant by using the as-prepared ZnO rods and found that the degradation was more effective using a 365 nm light source than using a 254 nm light source. This result confirms that the as-processed ZnO rods could be used directly under sunlight for the degradation of methyl violet present in polluted water. Our experimental results, confirmed that the sample with more oxygen defects shows better photocatalytic degradation of the dye molecule due to the involvement of oxygen vacancy defects and oxygen interstitials in the charge recombination process and helps in better catalytic reaction under a UV lamp.

1. Introduction

Zinc oxide (ZnO) has currently drawn intense global attention due to its projected application as an alternative photoanode to TiO_2 in Dye-Sensitized Solar cells [1,2]. Other major applications of nanostructured ZnO are as photocatalysts, sensors, and also as light emitting diodes [3]. Various attempts have been carried out in controlling the size and shape of ZnO nanocrystals, as it provides a better mode for investigating the dependence of electronic and optical properties on the size confinement and dimensionality. The large number of publications appearing in the area of ZnO based DSSCs, throw light on the increased use of ZnO and ZnO based nanomaterials as alternative photoanodes to TiO_2 in the Dye-Sensitized Solar cells [4–6]. In addition, the recent studies indicated that ZnO can also be used as a promising photocatalyst for the degradation of organic pollutants under UV/visible/solar irradiation [7–13]. Most of the photocatalytic or photodegradation studies using ZnO as a catalyst have been focussed on rhodamine B, methylene blue or methyl orange dyes, with a very few on methyl violet [14,15]. However, the important point to note is that in both the cases, the applications of ZnO are strictly dependent on its morphology, dimensionality, size, shape and surface defects [16].

Among the various multifarious synthesis techniques available for the preparation of ZnO nanostructures [3–6], sonochemical process [17,18] turned out to be a promising option due to its capability to control the purity, crystallinity and composition of the desired product, in addition to its cost effectiveness [18–22]. The available reports strongly suggested that careful control of synthetic parameters and growth conditions can result in ZnO nanostructures with exotic size, shape and morphology by the sonochemical process. In most of the cases, formation of ZnO occurred via the intermediate formation of $Zn(OH)_2$ and $[Zn(OH)_4]^{2-}$ [23,24]. In spite of the large number of information available on the growth of ZnO in various forms, there is still considerable uncertainty regarding the possible role of zinc hydroxide, its concentration, the mechanism by which

* Corresponding author at: Nano-Structured Materials Division, CSIR-Central Glass and Ceramic Research Institute (CSIR-CGCRI), 196, Raja SC Mullick Road, Jadavpur, Kolkata 700 032, India. Tel.: +91 33 24838082; fax: +9133 24730957.
E-mail addresses: psujathadevi@cgcri.res.in, psujathadevi@gmail.com (P.S. Devi).

http://dx.doi.org/10.1016/j.apcatb.2014.09.045
0926-3373/

zinc hydroxide converts to zinc oxide and the factors governing the product morphology. Our main objective was to optimize the reaction conditions to prepare ZnO rods at low temperature and correlate its formation with reaction parameters such as temperature, duration and concentration of the starting zinc hydroxide precursor. For this purpose, we have used sonication assisted chemical precipitation process using a weak base like NH_4OH to prepare zinc hydroxide. As a part of our on-going program on DSSC, we prepared ZnO flower, cubes and rods by both precipitation and sonochemical techniques and studied their performance as photoanodes in DSSC [25–28]. Further, we have also investigated the photocatalytic application of the synthesized materials for environmental applications. In here, we report the detailed growth process of ZnO rods and the photocatalytic degradation of a cationic dye methyl violet using the solution grown ZnO rods. The methyl violet (MV) is a typical example of industrially pertinent toxic cationic dye having a lot of detrimental effects on global lives. It is largely used as a purple dye in textile, leather, paint, in paper industries as tinter to give a visually bright appearance in paper, and testing pH ranges as an acid–base indicator [14,15,29–31]. Most of the reported photocatalytic studies of ZnO are on methylene blue and methyl orange by using UV light of 254 nm radiation. There are hardly any reports on the degradation of methyl violet dye using ZnO nanorods [14,15]. It is interesting to note that the UVC component of sunlight with wavelengths between 100 and 280 nm, is very energetic but is filtered out by the ozone layer, and never reaches earth whereas the UVA is long range radiation between 320 and 400 nm which is not readily absorbed by the ozone layer and 95% of it gets through and reach the earth's surface. Therefore, in this work we have investigated the photocatalytic degradation of methyl violet by solution processed ZnO rods using both two different wavelengths of UV lights such as 254 and 365 nm, respectively.

2. Experimental

2.1. Synthesis of ZnO

ZnO rods have been prepared from Zinc acetate dihydrate ($Zn(OAc)_2{\cdot}2H_2O$, 99.5%AR, Merck Ltd. Germany) as zinc source and ammonium hydroxide (30% GR, Merck Ltd. Mumbai, India) as a precipitating agent. Acetone (Merck Ltd. Germany) and ethanol (Merck Ltd. Germany) were used as washing liquid and dispersion medium, respectively, without further purification. All the reactions have been carried out in aqueous media using distilled water as a solvent.

Initially, precipitation was carried out using 0.1 M zinc acetate dihydrate solution and ammonium hydroxide as the precipitating agent under sonication (Ultrasonic power 250 W, ultrasonic frequency 25 kHz, probe diameter, 25 mm). A homogeneous white precipitate of zinc hydroxide was formed by the drop-wise addition of NH_4OH during sonication (2 h) until the pH of the zinc acetate solution was raised to 9.0 ± 0.5. Subsequently, the precipitate thus formed was centrifuged and dispersed in distilled water followed by heating at $80 \pm 5\,^{\circ}C$ for several hours on a magnetic stirrer with constant stirring to induce the nucleation and growth of zinc oxide. In order to elucidate and understand the conversion of precipitated zinc hydroxide to zinc oxide, we have varied the reaction durations and the precursor concentrations. In all the cases the reaction temperature was maintained at $80 \pm 5\,^{\circ}C$. The obtained products were further centrifuged at ~12,000 rpm and washed with distilled water and acetone followed by drying under an IR lamp. To investigate the effect of reaction duration on the nucleation and formation of ZnO from zinc hydroxide, an aqueous solution growth process was carried out by taking a 0.3 (w/v) % concentration of zinc hydroxide precursor solution in distilled water and heating the mixture at $80 \pm 5\,^{\circ}C$ for 2, 4 and 6 h, respectively, on a magnetic stirrer. Throughout the growth process, pH of the precursor solution was monitored very carefully. While the initial dispersion of zinc hydroxide in distilled water at room temperature shows a pH of 7 ± 0.5, but with an increase in temperature to $80 \pm 5\,^{\circ}C$, the solution becomes alkaline with a pH of 8 ± 0.5 due to more ionization at elevated temperatures. This high pH of the growth solution persists for 2–4 h and beyond which it decreases to 6 ± 0.5 after 6 h. The corresponding samples formed were denoted as S-1, S-2 and S-3, respectively, for convenience. In order to investigate the effect of concentration of the precursor at a fixed reaction duration of 6 h, the growth process has been repeated with a dilute (0.16 (w/v) %) concentration of the precursor hydroxide. It was observed that the final pH of both the precursor growth solution was around 6.0 ± 0.5. The corresponding sample formed is denoted as S-4 in rest of the manuscript.

2.2. Characterization

The dried powder was characterized by powder X-ray diffraction (XRD) analysis on a X'pert pro MPD XRD of PAN analytical with CuKα radiation ($\lambda = 1.5406$ Å). In order to understand the thermal decomposition nature of the samples, thermo gravimetric analysis (TGA) and differential scanning calorimetric (DSC) studies were carried out on the powder samples from room temperature to ~1000 °C at a heating rate of 10 °C/min on a NETZSCH 449C simultaneous thermal analyzer. In order to monitor the consequent changes in the morphology that may have appeared during the reaction, Scanning Electron Microscope (SEM) and Field Emission Scanning Electron Microscope (FESEM) studies were carried out on a LEO 430i (Carl Zeiss) Scanning Electron Microscope and Supra 35 VP (Carl Zeiss) Field-Emission Scanning Electron Microscope, respectively. The particle morphology and local crystallographic structure were studied by Transmission Electron Microscopy (TEM) and High-Resolution Transmission Electron Microscopy (HRTEM), respectively, on a Tecnai G2 30ST (FEI) high resolution transmission electron microscope operating at 300 kV. Fourier transform infrared (FTIR) spectra of the samples were recorded on a Nicolet 380 FTIR spectrometer using KBr. BET surface area of the samples were measured by nitrogen sorption isotherm process using Quantachrome twin surface area analyzer (NOVA 4000e). The absorption spectra were measured on a UV–Vis–NIR Spectrophotometer (Shimadzu UV-3600). The optical properties of the ZnO rods were further evaluated by recording the room temperature photoluminescence spectrum (PL) on a Steady State Spectrofluorometer (QM-40, Photon Technology International, PTI) using a 150 W Xenon lamp as an excitation source, at an excitation wavelength of 345 nm and a band pass of 5 nm. Raman Spectra were obtained using a Renishaw in via Reflex micro Raman spectrometer with an argon ion (514.6 nm) laser. The spectra were collected with a resolution of 1 cm^{-1}. The X band Electron paramagnetic resonance measurements of the powder samples were performed using a Bruker EMX spectrometer at room temperature and the microwave frequency was measured with a Hewlett-Packard 5246 L electronic counter. About 5 mg of each sample was taken in a quartz tube of 1 mm diameter. Instrumental parameters used for the measurement are frequency = 9.45 GHz, BO-field = 346 mT, BO-sweep = 200 mT, mod amplitude = 0.2 mT, and sweep time = 60 s.

2.3. Photocatalytic activity studies

After thorough characterization and property evaluation, the photocatalytic activity of few selected ZnO samples were studied by monitoring the photocatalytic degradation of 10^{-5} M methyl violet (MV) solution in presence of an 8W UV lamp (UVLS-28 EL Series) having an average light intensity of 0.6 mW/cm^2, excited at 365 nm (3.39 eV) and 254 nm (4.88 eV), respectively, using a very simple

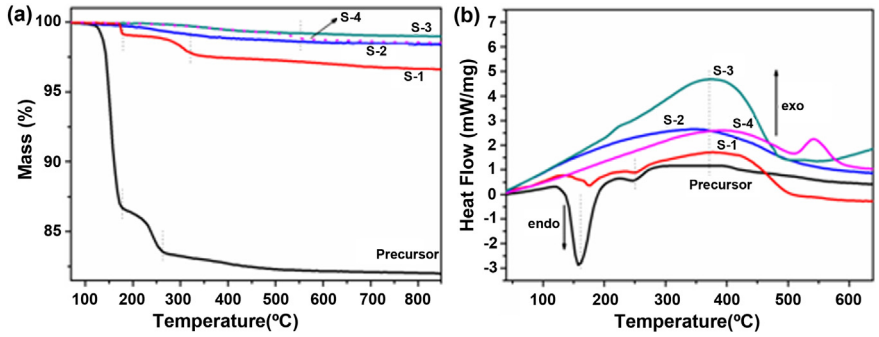

Fig. 1. (a) Thermogravimetric analysis and (b) Differential scanning calorimetric analysis of precursor and ZnO samples prepared at different reaction conditions.

indigenously built set up as shown in Fig. S1. Prior to monitoring the dye degradation, 25 mg ZnO sample was suspended in 50 ml MV dye solution of 10^{-5} M and was stirred thoroughly using a magnetic stirrer at room temperature for 15 min in the dark to equilibrate the homogenization of adsorption/desorption. The photocatalytic experiment was conducted at normal atmospheric condition at 28 ± 2 °C. We have performed all the photocatalytic degradation reactions at a natural pH of 6.5 ± 0.1 exhibited by the methyl violet dye solution itself and have not used any external acid/base for adjusting the pH to neutral. Degradation rate was measured by monitoring the change in the absorption maximum of the MV dye molecule at the maximum wavelength of 579 nm. Immediately after the illumination, the absorption changes were monitored by taking an aliquot of the solution from the mixture after centrifugation. The residual mixture was irradiated with 365 and 254 nm light and the absorbance changes were monitored at 579 nm at 15 min time intervals and the experiments were continued till the colour of the solution became colourless. Comparative studies were also performed using a reference catalyst, Degussa (P25) and also without any catalyst (blank experiment) under identical experimental set up as shown in Fig. S1. The extent of photocatalytic degradation was evaluated by the equation, degradation (%) = $(C_o - C_t)/C_o \times 100$, where C_o and C_t represent the initial absorbance and absorbance after 't' min reaction time at a λ_{max} of 579 nm. To study the adsorption property of the samples the same experimental conditions were repeated in dark for 150 min at room temperature.

3. Results and discussion

3.1. Structure and morphology

In order to understand the nature of decomposition of the precipitated zinc hydroxide, the thermal decomposition studies have been carried out as shown in Fig. 1a and b. As evident from Fig. 1a, the thermal decomposition characteristics of the products formed was very different from that of the starting precursor hydroxide. A rapid mass loss of 13.31% observed upto ~170 °C was ascribed to the dehydration of the precursor corresponding to the desorption of around 0.74 moles of H_2O. Further decomposition of $Zn(OH)_2$ continues upto 350 °C, followed by a stable weight corresponding to the formation of ZnO. The observed weight changes correspond to the possible formation of a precursor such as $Zn(OH)_2 \cdot 0.74H_2O$. Interestingly, the mass loss of sample S-1 occurs at a slightly higher temperature of ~174–340 °C giving rise to a weight loss of 3.14%. As the reaction proceeds further the mass loss gradually decreases to 1.32% and 0.73%, respectively, for the S-2 and S-3 samples. But a closer look at the thermal decomposition nature of all the products confirms the completion of the decomposition reaction at ~350 °C. The strong endotherm around 170 °C of the precursor sample corresponds to the decomposition of the precursor hydroxide as confirmed from the TGA results. The other endotherms exhibited by the hydroxide around 170 and 240 °C (Fig. 1b) exactly corresponds to the decomposition steps found in the TGA. The above decomposition steps were also present in the TGA and DSC curves of sample S-1 confirming the presence of undecomposed hydroxide in S-1. No endothermic peaks were present in the DSC curves of S-3 and S-4, confirming the complete conversion of the precursor hydroxide to the oxide. Interestingly, sample S-4 exhibited a two stage weight loss of ~0.4% at ~150 °C due to dehydration and a second mass loss of ~1.59% at slightly higher temperature of ~500 °C, indicating the presence of other polymorphic forms of zinc hydroxide that would have formed as intermediates in presence of excess water.

The quality of the products formed was monitored by the FTIR spectroscopy measured at room temperature (Fig. S2). The FTIR spectrum of the precursor hydroxide indicates strong stretching vibrations of hydrogen bonded hydroxyl groups at ca. 3492 and 3394 cm^{-1}, respectively [32]. The strong bands at 1396 cm^{-1} and 1554 cm^{-1} present in the IR spectrum of the precursor hydroxide are due to the symmetrical stretching of the C=O and C–O bonds, respectively, of unreacted surface carboxylate groups. The presence of O–H stretching vibrations of hydroxyl groups was also evident in the IR spectrum of S-1, S-2 and S-4 samples. The broad band around 3558 cm^{-1} and the weak band around 1617 cm^{-1} corresponds to defect related –OH and the O–H stretching vibration of molecularly adsorbed H_2O [32]. The strong absorption bands exhibited by S-2, S-3 and S-4 samples at ca. 550 cm^{-1} correspond to the Zn–O stretching frequency [33]. A careful observation of the IR spectra of both the samples prepared at 6 h revealed that S-4 shows a comparatively intense O–H stretching vibration band compared to S-3, which is in consistent with the TGA-DSC results confirming the presence of un-reacted hydroxides and hydroxyl complexes in hygroscopic S-4 sample.

The XRD patterns of the as-prepared precursor and the solution processed products prepared at different reaction conditions were compared as shown in Fig. 2. The major reflections in the XRD pattern of the as-prepared precipitate match well with the Joint Committee on Powder Diffraction Standards data file (No: 38-0385) of Wulfingite ε-$Zn(OH)_2$ [24]. Further, the XRD pattern also reveals the presence of trace amount of ZnO along with $Zn(OH)_2$. The as-prepared $Zn(OH)_2$ gradually disappeared during stirring the aqueous solution of the precursor at 80 ± 5 °C. This has been confirmed from the XRD results of the product that matches well with the reported pattern of wurtzite ZnO (JCPDS No: 36-1451) confirming the formation of ZnO. The major phase present at 2 h (S-1) was still zinc hydroxide with zinc oxide as a minor phase whereas sample S-2 prepared at 4 h consisted mainly of ZnO. The products formed in the S-3 and S-4 batches matched well with the reported ZnO pattern with a hexagonal wurtzite structure. In addition, very weak reflections corresponding to zinc hydroxide phase have also been observed in sample S-4 which also supports our

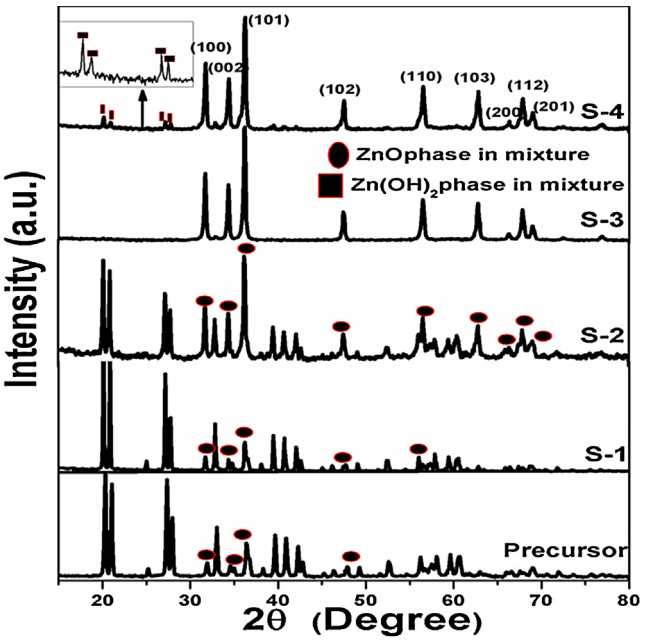

Fig. 2. XRD patterns obtained for the precursor and ZnO samples prepared at different reaction conditions.

other observations from IR and TGA. Only a negligible change in the lattice constant was observed for the products S-3 and S-4. The calculated lattice constants were, for S-3, $a = 3.253$ Å and $c = 5.215$ Å and for S-4 $a = 3.251$ Å and $c = 5.208$ Å, respectively. The intensity ratio ($I_{[1\,0\,0/0\,0\,2]}$) of all the as-prepared ZnO samples have been calculated, which varied as 1.43, 1.24, 1.21 and 1.32, respectively for samples S-1, S-2, S-3 and S-4, respectively. The corresponding standard value reported for bulk isotropic ZnO is 1.17. Any deviation from this value indicates particle anisotropy. Conversely, in our case we have observed a $I_{[1\,0\,0/0\,0\,2]}$) ratio which is higher than the standard value of 1.17 indicating a restricted growth along the 0 0 2 direction.

The observed morphological changes of the as-prepared hydroxide precursor at different reaction conditions are illustrated in Fig. 3(a–f). The as-prepared hydroxide did not exhibit any preferred morphology and exhibited chunks of solid as evident from Fig. 3a. Heating the dispersed hydroxide in water resulted in a simultaneous formation of long needle like structures concomitant with the formation of ZnO (Fig. 3b). It clearly indicates the appearance of needle like structures protruding from the hydroxide solid chunk. The FESEM of the 4 h heated sample indicated the presence of nearly rod shaped particles along with very few large chunks of particles (Fig. 3c). Further heating to 6 h, has resulted in the complete conversion of the entire as-prepared shapeless particles to rod shaped particles (Fig. 3d). At this condition, the thicker bundles get dispersed and separated. The higher magnification FESEM picture (Fig. 3e) shows a much closer examination of individual rods, where

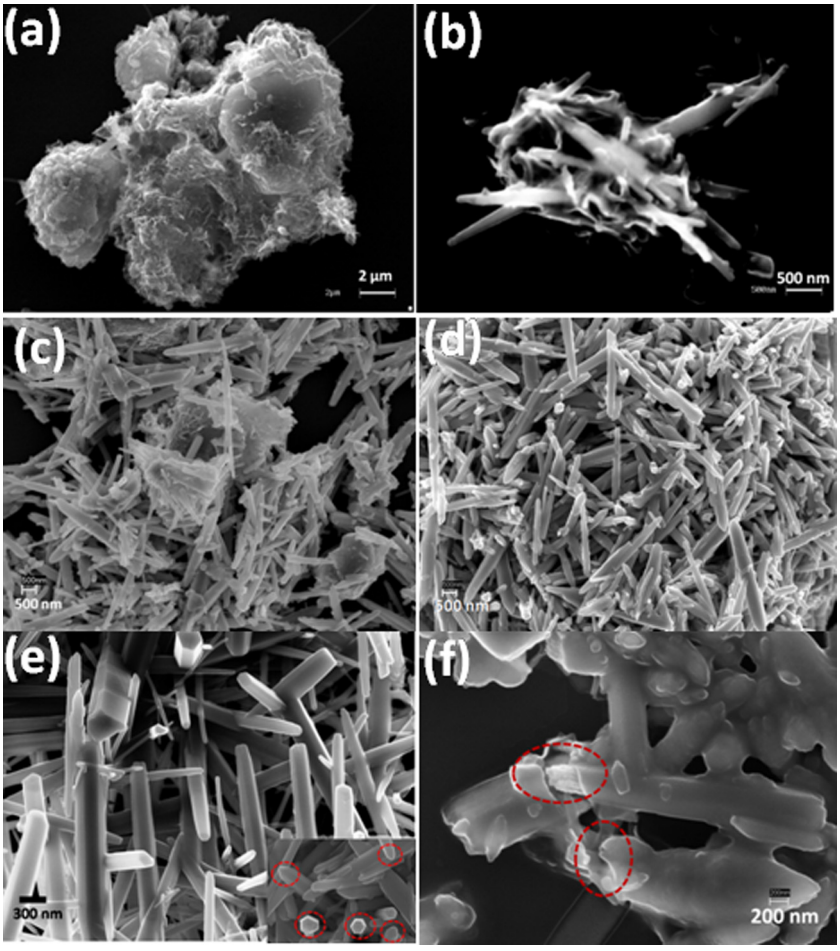

Fig. 3. SEM images of (a) as-prepared precursor, (b) S-1, (c) S-2, (d) S-3; FESEM images of (e) S-3 and (f) S-4.

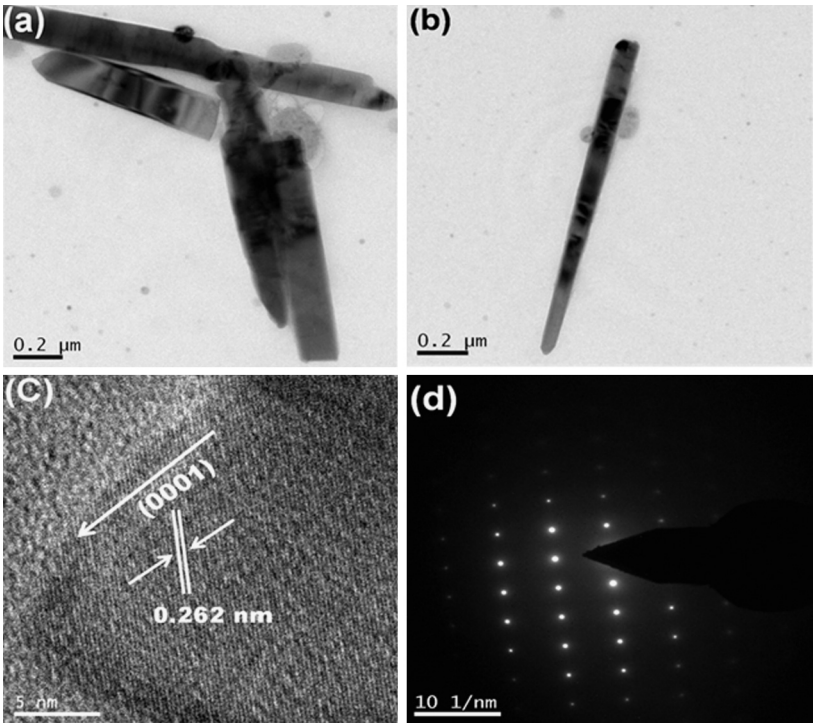

Fig. 4. (a and b) TEM images of rods, (c) HRTEM and (d) SAED pattern obtained for the ZnO prepared at optimized condition.

the hexagonal surface of the rods are evident. The tips of the rods are basically tapered while the base is of hexagonal shaped. Other experimental evidences confirmed that this change in morphology of the starting material is due to the formation of ZnO rods. Therefore, it could be confirmed that the rod shaped samples of ZnO were formed from zinc hydroxide during heating a colloidal dispersion of zinc hydroxide at 80 ± 5 °C at 6 h. It appears that increase in the reaction time has provided enough time for the complete decomposition of zinc-hydroxo complexes to form ZnO. But exceeding the reaction time beyond 6 h led to the aggregation of ZnO rods (Fig. S3). Based on the above observations, six hours of heating at 80 ± 5 °C has been fixed as the optimum condition required to grow ZnO rods from the sonochemically prepared zinc hydroxide precursor having an aspect ratio of 8–12.

A comparison of the morphology of the products at various stages gave direct evidence that:

(1) Initially ZnO nucleation occurs along with zinc hydroxide during the reaction of zinc acetate and ammonium hydroxide under sonication at room temperature, but the complete conversion of zinc hydroxide to ZnO rods required a higher temperature and longer reaction time.
(2) A concentration of 0.16 (w/v) % was not enough to induce the growth of ZnO rods under the same reaction duration as evident from the FESEM pictures shown in Fig. 3f.

The structure of ZnO rods prepared at optimized conditions i.e. S-3 sample was further characterized by transmission electron microscopy (TEM), high resolution transmission electron microscopy (HRTEM) and selected area electron diffraction (SAED) studies. In Fig. 4(a–d), the TEM pictures of the ZnO rods prepared at the optimized condition are presented. Few rods grown adjoining to each other are shown in Fig. 4a. Fig. 4b shows the image of a single rod with an aspect ratio of 9.52. The lattice planes separation indicated by the arrows in Fig. 4c is 0.262 nm, a value corresponding to the (0 0 2) plane of ZnO. The SAED pattern (Fig. 4d) and high resolution TEM analysis indicate a structure similar to the Wurtzite structure of ZnO with the growth along the [0 0 0 1] direction, the polar *c*-axis of the ZnO crystal lattice.

3.2. Optical properties

The room temperature photoluminescence (PL) spectra of ZnO prepared at different reaction conditions are presented in Fig. 5. The PL spectrum of S-1, S-2, S-3 and S-4 samples exhibited a near-band-edge emission (NBE) at 383 ± 1 nm (~3.24 eV) and a broad visible luminescence in the 450–700 nm range with a band maximum (λ_{max}) at 565 ± 3 nm. ZnO usually exhibits two emission peaks, a sharp and highly intense emission in the near UV and a relatively weaker and broader emission in the visible region [34–36]. The NBE emission has been reported to

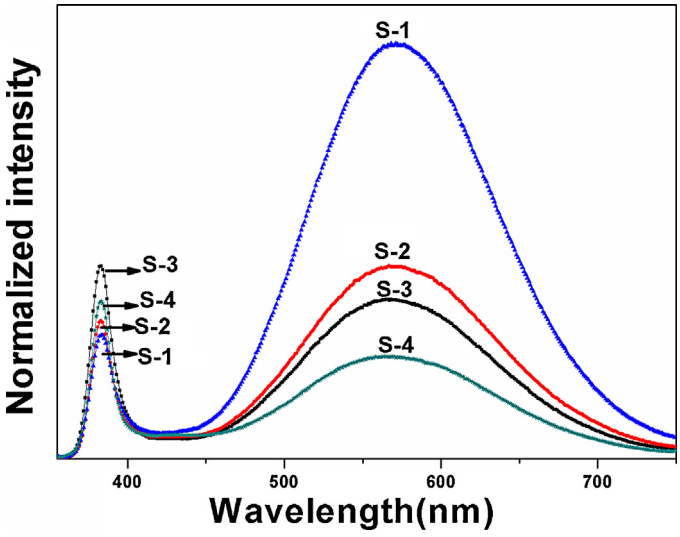

Fig. 5. Room temperature photoluminescence spectra obtained for the ZnO samples prepared at different reaction conditions.

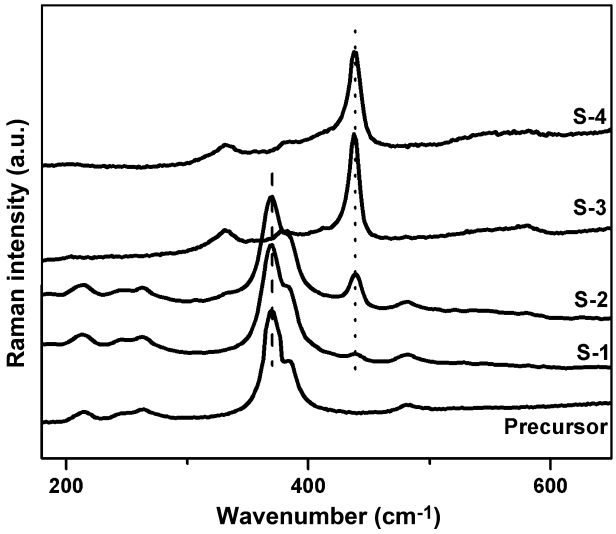

Fig. 6. Raman spectra obtained for the precursor and ZnO samples prepared at different reaction conditions.

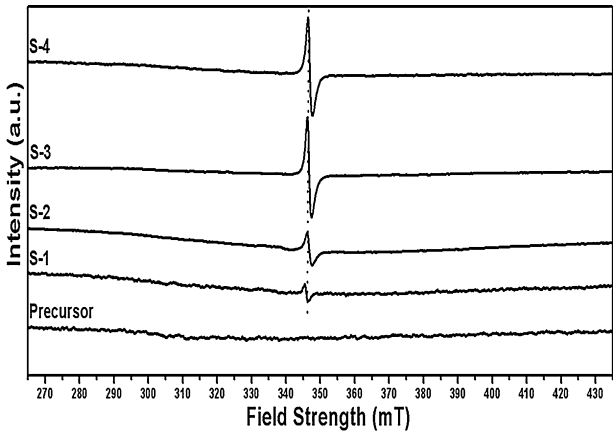

Fig. 7. Room temperature Electron Paramagnetic Resonance spectra obtained for the precursor and ZnO samples prepared at different reaction conditions.

originate from the direct recombination of excitons and the visible emission from the radiative recombination from different defect states like oxygen vacancies (V_o), zinc vacancies (V_{Zn}), zinc interstitials (Zn_i), oxygen interstitials (O_i) or impurity levels present in the samples depending on their preparation conditions [34–36]. In our case, S-1 exhibited a weak NBE (383 ± 1 nm) and a strong visible emission around $\sim 565 \pm 3$ nm. But as the reaction proceeds the NBE gradually increases with decrease in visible emission with sample S-3 exhibiting maximum NBE. This change may be due to the formation of crystalline ZnO rods with reduced surface defects at the expense of gradual decomposition of hydroxide precursor with time [36]. It can be seen from Fig. 5 that the relative intensity of near band edge emission to the visible emission I_{NBE}/I_{Vis} varies from 0.29 to 0.71 to 1.26 to 1.54 for S-1, S-2, S-3 and S-4, samples respectively. The higher I_{NBE}/I_{Vis} value of S-4 sample indicates the presence of lower defect concentration as compared to S-3 sample. In order to unravel the reason behind this change, the PL spectrum in the broad defect related visible region was deconvoluted into two Gaussian peaks located at 560 nm (denoted by D1) and 618 nm (denoted by D2), respectively (Fig. S4). In our previous work, we have attributed the band at 560 nm to double ionized oxygen vacancy ($V_o^{\bullet\bullet}$) and the band at 618 nm to chemisorbed/interstitial oxygen [28,34–36]. The different reaction conditions also induce variation in defect concentration as revealed from the intensity of the deconvoluted peaks D1 and D2 in the PL spectra of each sample (Fig. S4).

3.3. Raman and electron paramagnetic resonance (EPR) studies

In order to further access the crystal quality of the prepared ZnO, we have also monitored the changes in the Raman spectra with the variation in the reaction conditions. Fig. 6 represents the Raman spectrum of ZnO samples prepared at different reaction conditions. We observed a strong peak $\sim 370\ cm^{-1}$ belonging to A_1 (Transverse-Optical, TO) with three additional small peaks located around 215, 263, 484 cm^{-1} indicating the presence of zinc hydroxide phase [37,38] in S-1 and S-2 samples. As the reaction continues the suppressed peak at $\sim 438\ cm^{-1}$ of sample S-1 and S-2 gets sharper and stronger turning into a dominant peak in S-3 and S-4 samples, which is attributed to Raman-active E_2 (High) mode, the characteristic Raman band of hexagonal Wurtzite phase of ZnO [37–39]. The Raman spectrum of S-3 and S-4 samples also exhibited other characteristic bands at $\sim 331\ cm^{-1}$ attributed to the 2-E_2(M) modes and the peaks at ~ 377 and 411 cm^{-1} assigned to the A_1 (Transverse-Optical, TO) and E_1(Transverse-Optical, TO) mode respectively related to multiphonon process and also a plateau at 580 cm^{-1} assigned to the E_1(Longitudinal Optical, LO) mode representing the scattering from defect levels and impurities present in the samples [39]. A gradual sharp increase of E_2 (High) peak intensity as compared to the other Raman peaks with increase in reaction duration further confirms the phase transformation from zinc hydroxide to zinc oxide with improved crystallinity.

In order to understand the origin of the defects exhibiting visible emission in the room temperature PL data, EPR studies have been carried out on all the samples as shown in Fig. 7. All the samples exhibited a strong single EPR signal at $g = 1.954 \pm 0.001$. In order to rule out the presence of singly ionized oxygen vacancies in our samples, we carried out magnetic measurements at room temperature (RT) on all the samples. All the samples exhibited diamagnetism at RT, giving an indirect evidence of the absence of either paramagnetic singly ionized oxygen vacancies or zinc interstitials in our samples. The observed EPR signal at 1.954 ± 0.001 could be assigned to shallow donor centres related to the incorporation of hydrogen in the solution processed ZnO [28,40–43]. It is anticipated that the incorporation of hydrogen during growth process was higher in S-4 sample (as revealed from experimental results) which acts as shallow donor and passivate the double ionized oxygen vacancy site [43] giving rise to less vacancy defect states as compare to S-3 sample.

3.4. Proposed reaction and growth mechanism of ZnO rods

ZnO, an amphoteric semiconducting oxide could easily be formed by the hydrolysis of various zinc salts at different pH and temperature depending on the zinc salt precursor, its concentration, pH, temperature etc. In this work, we have used zinc acetate and a mild alkali NH_4OH to prepare ZnO nanostructures. The powder X-ray diffraction patterns collected from the precipitate formed during the reaction of zinc acetate and NH_4OH confirmed it to be ε-$Zn(OH)_2$. The crystalline ε-$Zn(OH)_2$ is reported to be thermodynamically metastable compared to ZnO at 25 °C [24]. However, the rate of transformation of ε-$Zn(OH)_2$ to ZnO is negligible at RT. This is due to the endothermic nature of the decomposition of ε-$Zn(OH)_2$ to ZnO as has been evident from the DSC data shown in Fig. 1b. Moezzi et al., reported that, due to the low solubility of ε-$Zn(OH)_2$ in water it required a temperature of 100 °C for its decomposition and subsequent conversion to ZnO [24]. But our experimental results confirmed that a temperature of 80 ± 5 °C was sufficient to induce the transformation of ε-$Zn(OH)_2$ to ZnO. This could be due to the

high reactivity of ε-$Zn(OH)_2$ formed during the sonochemical process. It was further evident that a small amount of $Zn(OH)_2$ was still present in the reaction product up to a duration of 4 h. So it was anticipated that a longer reaction time was necessary for the complete conversion of $Zn(OH)_2$ to ZnO, probably via the formation of a $Zn(OH)^+$ complex as shown below. The plausible reaction mechanism for the formation of ZnO rods could be predicted as follows:

The hydrolysis of zinc acetate and NH_4OH in distilled water, are shown in reactions (1–3).

$$Zn(CH_3COO)_2{\cdot}2H_2O \rightarrow Zn^{2+} + 2CH_3COO^- + 2H_2O \quad (1)$$

$$CH_3COO^- + H_2O \rightarrow CH_3COOH + OH^- \quad (2)$$

$$NH_3 + H_2O \rightarrow NH_4^+ + OH^- \quad (3)$$

On addition of ammonium hydroxide to zinc acetate solution, zinc hydroxide $Zn(OH)_2$ or tetrahydroxozincate ion $[Zn(OH)_4]^{2-}$ may be formed depending on the availability of OH^- ions as shown in Eqs. (4) or (5). In our case, evidences confirmed the formation of white precipitate of $Zn(OH)_2$. As discussed in the experimental section, we have dispersed the hydroxide precipitate in water, so as to form various concentrations of the precursor solution. The pH of the dispersion before heating was around neutral (7 ± 0.5), whereas on heating the pH of the dispersion slowly increased to around (8 ± 0.5) and finally it reduced to (6 ± 0.5). Therefore it was anticipated that on heating the insoluble hydroxide in water, it would have been hydrolyzed to form soluble $Zn(OH)^+$ as per Eq. (8) resulting in an increase in pH of the solution as suggested by Randy et al. [44]. This has also been confirmed by the appearance of a comparatively clear solution during heating. Li et al. proposed that at a pH of 10–12, the most ideal growth unit for the nucleation of ZnO to be $Zn(OH)_4^{2-}$ [45], but in our case, as the pH of the solution during the reaction was noted as 8 ± 0.5, $Zn(OH)^+$ could be the probable active growth unit [44]. At a higher reaction temperature of 80 ± 5 °C, the concentration of $Zn(OH)^+$ active growth unit increases which leads to the rapid formation of ZnO at a faster rate as shown in Eqs. (8–11).

$$Zn^{2+} + 2OH^- \rightarrow Zn(OH)_{2(s)} \quad (4)$$

$$Zn^{2+} + 4OH^- \rightarrow [Zn(OH)_4]^{2-} \quad (5)$$

$$Zn(OH)_{2(s)} \rightarrow Zn(OH)_{2(aq)} \quad (6)$$

$$Zn(OH)_{2\,(aq)} \xrightarrow{\Delta} Zn^{2+}_{(aq)} + 2OH^-_{(aq)} \quad (7)$$

$$Zn(OH)_{2(aq)} \rightarrow Zn(OH)^+{}_{(aq)} + OH^-{}_{(aq)} \quad (8)$$

$$Zn^{2+} + OH^-{}_{(aq)} \rightarrow Zn(OH)^+{}_{(aq)} \quad (9)$$

Throughout the growth process the solution pH was slightly lower for the diluted precursor solution, but finally it becomes 6 ± 0.5.

In dilute solution the probable mechanism may be as follows:

$$Zn^{2+}{}_{(aq)} + H_2O_{(liq)} \rightarrow Zn(OH)^+{}_{(aq)} + H^+{}_{(aq)} \quad (10)$$

Finally in both cases,

$$Zn(OH)^+_{(aq)} + H_2O_{(liq)} \xrightarrow{\Delta} ZnO_{(s)} + H_3O^+_{(aq)} \quad (11)$$

The formation of H_3O^+ renders the ultimate mixture slightly acidic (pH 6 ± 0.5).

ZnO is a polar crystal with each Zn^{2+} lying in a tetrahedral group of four oxygen ions and O^{2-} lies in a hexagonal close packed system. Zn and oxygen atoms are arranged alternatively along the *c*-axis with a Zn terminated (0 0 0 1) top surface and an O^{2-} terminated (0 0 0 $\bar{1}$) bottom surface. One of the most profound factors determining the morphology in a crystal growth process involves the relative surface activities of various growth facets under the given conditions. The velocities for growth are reported as polar (0 0 0 1) > (1 0 $\bar{1}$ 1) > nonpolar (1 0 $\bar{1}$ 0) [46]. Interestingly, the surface energies (*E*) of the facets in ZnO crystals also follow the sequence $E(0\,0\,0\,1) > E(1\,0\,\bar{1}\,1) > E(1\,0\,\bar{1}\,0)$ which is the same order as the crystal growth rates. The more rapid the growth rate, the quicker be the disappearance of the basal plane (0 0 0 1) leading to the formation of rod like ZnO with pointed or tapered shapes. In Fig. 8 the schematic of ZnO rods formation at 80 ± 5 °C by the stirring cum heating process is presented.

3.5. Photocatalytic properties of the ZnO rods

In order to evaluate the application of the solution grown ZnO rods as a catalyst for the photodegradation of the textile pollutant, methyl violet, we have carried out their photocatalytic degradation

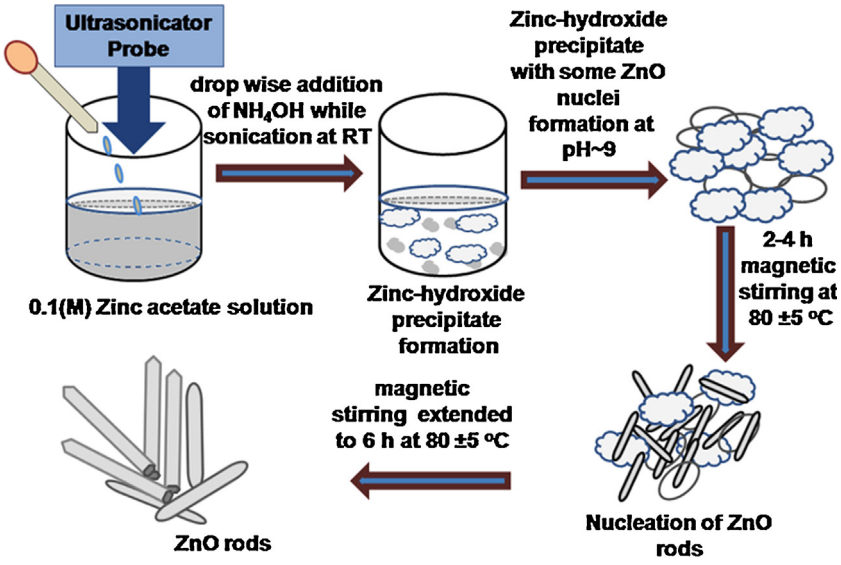

Fig. 8. Proposed schematic of the growth of ZnO rods prepared at the optimized condition.

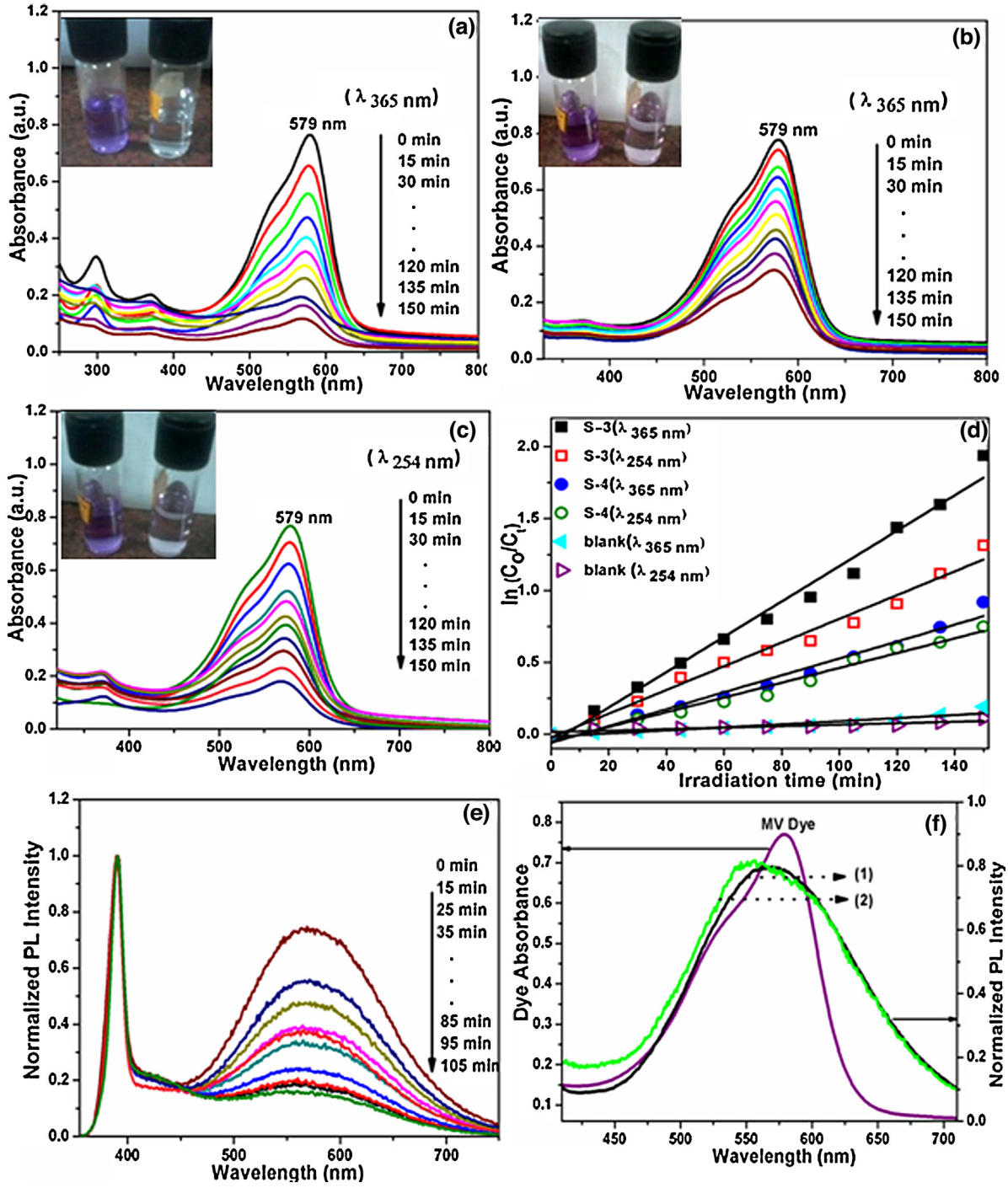

Fig. 9. UV–Vis absorbance spectral changes of the Methyl Violet dye monitored during the phocatalytic degradation by the addition of (a, c) S-3 and (b) S-4 under illumination of UV lamp (8 W) at different excitation wavelength; Inset shows photos of MV dye solution in presence of (a, c) S-3 and (b) S-4 before and after prolonged illumination; (d) comparative photocatalytic degradation rate of S-3, S-4 and blank experiment (without using any photocatalyst) at different excitation wavelengths, (e) Corresponding room temperature PL emission data of dye adsorbed S-3 under UV irradiation, (f) comparative absorption–emission study of dye and S-3 (1) before and (2) after the dye adsorbed onto it.

kinetics at room temperature in presence of UV light using two different wavelengths of 365 nm (3.39 eV) and 254 nm (4.88 eV), respectively, of which 3.39 eV is close to the direct band gap energy of the photocatalyst ZnO (~3.36 eV) and the other is of higher energy than the band gap energy. A blank experiment was also performed at identical experimental conditions without using any catalyst to monitor the auto-photocatalytic property of the dye. Moreover, the catalytic performance of our samples were compared with the photocatalytic performance of a reference catalyst Degussa (P25) under identical experimental set up and conditions as shown in Fig. S1.

In Fig. 9(a–c) and Fig. S5, the variation of the absorbance of methyl violet dye solution in presence of S-3 and S-4 samples under UV light exposures of 365 and 254 nm, respectively, are presented. It can be seen that the characteristic absorption band of the dye at 579 nm gradually decreased as a function of irradiation time. Fig. 9a and b show an obvious difference in the degradation of MV in presence of S-3 and S-4 samples, respectively,

when exposed to 365 nm UV light, where S-3 exhibits a better photocatalytic activity(Fig. 9a). Similarly, there is also an obvious difference in the degradation of MV on exposure to 254 nm light as evident from Fig. 9c and Fig. S5. The degradation rate of different experiments has been plotted in Fig. 9d along with that of the blank experiment. From Fig. 9d, it appears that the degradation rate varies as S-3 ($\lambda_{365\,nm}$) > S-3 ($\lambda_{254\,nm}$) > S-4 ($\lambda_{365\,nm}$) > S-4 ($\lambda_{254\,nm}$) > blank ($\lambda_{365\,nm}$) > blank ($\lambda_{254\,nm}$). More precisely, the as-prepared S-3 sample exhibited a better photocatalytic activity compared to S-4 resulting in 88% degradation at 150 min. When we compared the photocatalytic activity of ZnO with that of a reference catalyst P25, it has become evident that the photocatalytic degradation of MV was better in presence of P25 (90 min. degradation time) when used a light of $\lambda_{365\,nm}$ whereas our sample performed better (79% at 150 min) compared to P25 (only 71% at 150 min.) when used a $\lambda_{254\,nm}$ light source (Fig. S6). While comparing the photocatalytic performance of as-prepared S-3 and S-4 samples under identical conditions of light exposure, the performance of S-4 sample was inferior to S-3. This has been attributed to the enhanced incorporation of shallow donor in S-4, as revealed through EPR measurements. The shallow donor sites being positively charged located on the surface served as binding sites for anionic dyes [12]. But, here, we have used a weakly acidic cationic dye methyl violet; its degradation rate was retarded as the increasing shallow donor concentration passivates the vacancy defects and inhibits the photogenerated holes to take part in the dye degradation process. In order to evaluate the adsorption nature of the synthesized ZnO rods, the suspensions were stirred in the dark to ensure adsorption–desorption equilibrium. The MV solution exhibited only a mild decrease in absorbance due to adsorption as shown in Fig. S7, in comparison to the photocatalytic degradation data shown in Fig. S6. When we have compared the photocatalytic degradation of the MV alone without any photocatalyst, the observed overall degradation was less than 10% while using a 365 nm UV light source. Interestingly, under 254 nm UV light irradiation, the performance was still inferior. The above results confirmed that the MV does not exhibit any reasonable photodegradation under exposure to UV light that has been used in these experiments. On the contrary, presence of a small amount of the synthesized defect enriched photocatalyst ZnO promoted the photodegradation of MV extensively thereby confirming the potential of the solution synthesized ZnO rods in removing the pollutant MV from water.

To study the reusability of the as-prepared photocatalyst S-3, the photoreaction mixture after exposure to UV light irradiation for 150 min was centrifuged at ~11,000 rpm and washed properly with distilled water and ethanol for several times in an ultrasonication bath, followed by drying at 70 °C in an oven. The recovered sample was again reused for photocatalytic application keeping the other parameters constant. After using the catalyst for three successive cycles also, the performance was not affected much as shown in Fig. S8.

In order to investigate whether the visible emission exhibited by ZnO is sensitive to the presence of methyl violet, and whether defects are playing any role in the dye degradation process, we have measured the emission spectra of S-3 sample dispersed in aqueous solution of the dye (Fig. 9e). The intensity of the defect related emission decreases with time while no change in the NBE emission (Fig. 9e) was noticed. It is also interesting to note that the quenching of the emission occurs only after excitation of the sample with the source UV lamp, and once the irradiation was stopped the sample retains the native characteristic defect emission as evident from Fig. 9e. Fig. 9f shows the dye absorbance and defect related visible emission of S-3 sample before and after dye adsorption. The involvement of defects during the photodegradation is very clear as there is a strong overlap between the dye absorbance and the defect related emission of ZnO. This result indicates the role of defects in enhancing the photocatalytic activity of ZnO.

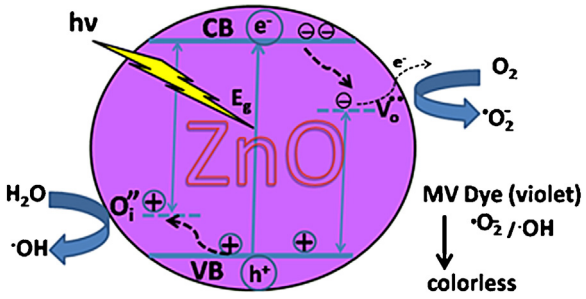

Fig. 10. Schematic representation of MV dye degradation using ZnO as a photocatalyst under illumination with UV light.

3.6. Photocatalytic activity and mechanism

The key steps involved in the mechanism of a heterogeneous photocatalysis on the surface of ZnO are charge-carrier generation, charge-carrier trapping, charge-carrier recombination and finally the photocatalytic degradation of the organic pollutant [47]. In order to understand the photocatalytic activity exhibited by the solution grown ZnO rods, we have looked into various parameters that in principle control the photocatalytic activity such as phase purity, particle size, surface area, surface hydroxyl groups, surface defects and their nature [8,9,47,48]. The BET surface areas of S-3 and S-4 samples were 6.81 and 7.2 m^2/g, respectively. The photocatalytic activity of the above samples, on the other hand, did not follow a similar trend as their photocatalytic degradation behaviour (Table S1). In spite of the smaller surface area, the degradation efficiency of S-3 (88%) was much higher than that of S-4 (64%). Next, we looked into the growth orientation of the derived rods. The (0 0 0 1) crystal plane of ZnO has been reported to exhibit superior photocatalytic activity compared to other crystal planes [48]. Our XRD results did not reveal any preferred growth along the 0 0 2 direction, though TEM confirmed the restricted growth of rods along 0 0 0 2 direction resulting in tapered ends. The crystal plane intensity ratio (100/002), also did not confirm a preferred orientation along 002 plane (Table S1). The above observations imply that the enhanced photocatalytic activity of S-3 sample is neither related to surface area nor to the polar crystal plane orientation effect. Few earlier reports suggested that the presence of defects in ZnO promote its photocatalytic activity, as defect could enhance the charge separation which in turn restrains the loss due to charge recombination [16,33,49].

Upon irradiation of ZnO rods by UV light of energy equivalent or greater than the bandgap energy of ZnO (E_g, 3.2 eV), electrons (e_{cb}^-) are excited from the valence band (VB) to the conduction band (CB), simultaneously leaving behind the same number of holes (h_{vb}^+) in the VB [47,33] and thereby forming electron–hole pair as shown in Fig. 10 and Eq. (12). This completes the charge-carrier generation step.

$$ZnO + h\nu \rightarrow e_{cb}^- + h_{vb}^+ \quad (12)$$

In the case of a defect free ZnO, the photogenertaed electrons and holes undergo fast recombination both in the bulk and on the surface. Therefore, it is important for the trapped electrons in the CB to be scavenged by an electron acceptor to suppress its recombination with the trapped hole. The PL studies on our samples confirmed the presence of two different kinds of oxygen defects on the surface as doubly ionised oxygen vacancies and oxygen interstitials(O_i). It has been reported that doubly ionised oxygen vacancies could act as electron acceptors which could trap the photogenerated electrons

temporarily to reduce the surface recombination and the interstitial oxygen could act as shallow trappers of photogenerated holes and thus both the defects are beneficial for efficient separation of holes and electrons and thereby restrain the recombination as shown below in Eqs. (13–16) [33].

$$V_O^{\cdot\cdot} + e_{cb}^{-} \rightarrow V_O^{\cdot} \quad (13)$$

$$V_O^{\cdot} + O_2 \rightarrow V_O^{\cdot\cdot} + {}^{\cdot}O_2^{-} \quad (14)$$

$$O_i'' + h_{vb}^{+} \rightarrow O_i' \quad (15)$$

$$O_i' + OH^{-} \rightarrow O_i'' + {}^{\cdot}OH \quad (16)$$

Through the reduction of molecular O_2 with electron, via the oxygen defects, reactive superoxide radical anions, $^{\bullet}O_2^{-}$ could be formed as shown in Eq. (14). Similarly, •OH free radicals are expected to be formed as per Eqs. (15 and 16) through the interaction of positive holes, oxygen interstitials and water. It is anticipated that the intermediate formed free radicals such as oxygen super oxide radical, hydroxyl radical and the positive holes are strong oxidising agents which helps in effective oxidation of the pollutant molecules ultimately resulting in efficient photodegradation. Zheng et al. suggested that the separation efficiency of oxygen vacancy defects is greater than that of oxygen interstitials based on band bending approximation [33] and hence oxygen vacancy defects are believed to suppress the recombination more effectively than oxygen interstitials. Therefore, we believe that the existence of doubly ionised oxygen vacancies as surface defects played a vital role in the enhanced photocatalytic activity of the solution grown ZnO rods. It is worth mentioning here, the high aspect ratio of prepared ZnO rods that could have helped in maintaining high level of surface defects on these rods. It may be noted that, the above mentioned mechanisms are expected to occur when the photocatalyst is excited with UV light of wavelength less than 400 nm. On the contrary, under the visible light with $\lambda > 420$ nm, the degradation of dye pollutant is expected to occur through photosensitized degradation, through electron injection from excited state dye molecule to the CB of ZnO [47,50]. Since we have used UV lights of $\lambda < 380$ nm, the observed photodegradation of the MV solution in presence of the ZnO rods is believed to be solely due to the photocatalytic activity of the prepared ZnO rods and not due to the photosensitized degradation of the MV molecule. It is interesting to note that, in our case photon energy (3.39 eV) close to the band gap energy of the photocatalyst (3.36) was more effective in reducing the recombination loss which in turn facilitated the photodegradation process of the dye more effectively as demonstrated above.

4. Conclusions

In summary, we have monitored the aqueous solution growth process of ZnO rods starting from zinc hydroxide that has been formed during the ultrasonic precipitation of zinc acetate precursor with ammonium hydroxide. While carrying out the growth process two important reaction parameters were optimized-duration of the reaction and concentration of the precursor. The conditions required to form ZnO rods were optimized as heating a 0.3 (w/v) % water dispersion of zinc hydroxide at $80 \pm 5\,^{\circ}C$ for 6 h. Further, we also investigated the photocatalytic degradation of methyl violet, which is a well known textile pollutant by using the as-prepared ZnO rods and found that the degradation was more effective using a 365 nm light source than using a 254 nm light source. We also investigated the influence of native defects on the photocatalytic activity of the as-prepared ZnO samples. We found that energy close to the bandgap energy of the ZnO (3.36 eV) and the existence of doubly ionised oxygen vacancies as surface defects played a vital role in the enhanced photocatalytic activity of the solution grown ZnO rods.

Acknowledgements

SM is indebted to the University Grants Commission, Govt. of India for the award of Senior Research Fellowships through the National Eligibility Test. PSD acknowledges Ministry of New and Renewable Energy (MNRE) for financial support under CSIR-TAPSUN (No: GAP 0339) programme. PPD acknowledges the financial support from MNRE to carry out the PhD program. The authors thank the Materials Characterization Division for their help. We thank the reviewers for their constructive criticism and comments that helped us to improve the manuscript considerably.

Appendix A. Supplementary data

Supplementary material related to this article can be found, in the online version, at http://dx.doi.org/10.1016/j.apcatb.2014.09.045.

References

[1] M. Gratzel, J. Photochem. Photobiol. C: Photochem. Rev. 4 (2003) 145–153.
[2] A. Hagfeldt, G. Boschloo, L. Sun, L. Kloo, H. Pattersson, Chem. Rev. 110 (2010) 6595–6663.
[3] L.S. Mende, J.L.M. Driscoll, Mater. Today 10 (2007) 40–48.
[4] J.A. Anta, E. Guillen, R.T. Zaera, J. Phys. Chem. C 116 (2012) 11413–11425.
[5] H.Y. Lai, Y.C. Lin, W.H. Chen, G.J. Chen, W.C. Kung, R. Vittal, K.C. Ho, J. Mater. Chem. 20 (2010) 9379–9385.
[6] F. Xu, L. Sun, Energy Environ. Sci. 4 (2011) 818–841.
[7] X. Wang, Q. Zhang, Q. Wan, G. Dai, C. Zhou, B. Zou, J. Phys. Chem. C 115 (2011) 2769–2775.
[8] C. Hariharan, Appl. Catal. A: Gen. 304 (2006) 55–61.
[9] B.M. Rajbongshi, S.K. Samdarshi, Appl. Catal. B: Environ. 144 (2014) 435–441.
[10] Y. Lv, W. Yao, X. Ma, C. Pan, R. Zong, Y. Zhu, Catal. Sci. Technol. 3 (2013) 3136–3146.
[11] J. Wang, P. Liu, X. Fu, Z. Li, W. Han, X. Wang, Langmuir 25 (2009) 1218–1223.
[12] F. Liu, Y.H. Leung, A.B. Djurišicć, A.M.C. Ng, WK, J. Phys. Chem. C 117 (2013) 12218–12228.
[13] G. Zhang, X. Shen, Y. Yang, J. Phys. Chem. C 115 (2011) 7145–7152.
[14] S. Ghorai, A. Sarkar, M. Raoufi, A.B. Panda, H. Schönherr, S. Pal, ACS Appl. Mater. Interfaces 6 (2014) 4766–4777.
[15] J.H. Sun, S.Y. Dong, Y.K. Wang, S.P. Sun, J. Hazard. Mater. 172 (2009) 1520–1526.
[16] X. Jhang, J. Qin, Y. Xue, P. Yu, B. Zhang, L. Wang, R. Liu, Sci. Rep. 4 (2014), 4596 (1–8).
[17] J.H. Bang, K.S. Suslick, Adv. Mater. 22 (2010) 1039–1059.
[18] A. Khorsand Zak, W.H. Majid, H.Z. Wang, R. Yousefi, A. Moradi Golsheikh, Z.F. Ren, Ultrason. Sonochem. 20 (2013) 395–400.
[19] P. Mishra, R.S. Yadav, A.C. Pandey, Ultrason. Sonochem. 17 (2010) 560–565.
[20] S.H. Jung, E. Oh, K.H. Lee, Y. Yang, C.G. Park, W. Park, S.H. Jeong, Cryst. Growth Des. 8 (2008) 265–269.
[21] M. Palumbo, S.J. Henley, T. Lutz, V. Stolojan, S.R.P. Silva, J. Appl. Phys. 104 (2008) 074906 1-6.
[22] S.S. Warule, N.S. Chaudhari, J.D. Ambekar, B.B. Kale, M.A. More, J. Cryst. Eng. Commun. 11 (2009) 2776–2783.
[23] M. Wang, Y. Zhou, Y. Zhang, S.H. Hahn, E. Kim, J. Cryst. Eng. Commun. 13 (2011) 6024–6026.
[24] A. Moezzi, M. Cortie, A. McDonagh, Dalton Trans. 40 (2011) 4871–4878.
[25] A. Jana, N.R. Bandyopadhyay, P.S. Devi, Solid State Sci. 13 (2011) 1633–1637.
[26] A. Jana, P.S. Devi, A. Mitra, N.R. Bandyopadhyay, Mater. Chem. Phys. 139 (2013) 431–436.
[27] A. Jana, P.P. Das, S. Agarkar, P.S. Devi, Solar Energy 102 (2014) 143–151.
[28] P.P. Das, S. Agarkar, S. Mukhopadhyay, M. Unnikrishnan, S.B. Ogale, P.S. Devi, Inorg. Chem. 53 (2014) 3961–3972.
[29] A. Mittal, V. Gajbe, J. Mittal, J. Hazard. Mater. 150 (2008) 364–375.
[30] K. Elass, A. Laachach, A. Alaoui, M. Azzi, Appl. Clay Sci. 54 (2011) 90–96.
[31] J.S. Wu, C.H. Liu, K.H. Chub, S.Y. Suen, J. Membr. Sci. 309 (2008) 239–245.
[32] H. Noei, H. Qiu, Y. Wang, E. Löffler, C. Wöll, M. Muhler, J. Phys. Chem. Chem. Phys. 10 (2008) 7092–7097.
[33] Y. Zheng, C. Chen, Y. Zhan, X. Lin, Q. Zheng, K. Wei, J. Zhu, Y. Zhu, Inorg. Chem. 46 (2007) 6675–6682.
[34] A.B. Djurisic, Y.H. Leung, Small 2 (2006) 944–961.
[35] A.B. Djurisic, Y.H. Leung, K.H. Tam, Y.F. Hsu, L. Ding, W.K. Ge, Y.C. Zhong, K.S. Wong, W.K. Chan, H.L. Tam, K.W. Cheah, W.M. Kwok, D.L. Phillips, Nanotechnology 18 (2007) 095702.
[36] B. Panigrahy, M. Aslam, D.S. Misra, M. Ghosh, D. Bahadur, Adv. Funct. Mater. 20 (2010) 1161–1165.
[37] N. Morales-Flores, R. Galeazzi, E. Rosendo, T. Diaz, S. Velumani, U. Pal, Adv. Nano Res. 1 (2013) 59–70.
[38] H. Zhou, H. Alves, D.M. Hofmann, W. Kreigseis, B.K. Meyer, G. Kaczmarczyk, A. Hoffmann, Appl. Phys. Lett. 80 (2002) 210–212.

[39] Y. Zhang, Y. Liu, L. Wu, H. Li, L. Han, B. Wang, E. Xie, Appl. Surf. Sci. 255 (2009) 4801–4805.
[40] A. Janotti, C.G. Van de Walle, Rep. Prog. Phys. 72 (2009), 126501 1-29.
[41] L. Jinpeng, L. Chundong, J. Belbruno, J. Cryst. Eng. Commun. 15 (2013) 5620–5625.
[42] G.A. Shi, M. Saboktakin, M. Stavola, S.J. Pearton, Appl. Phys. Lett. 85 (2004) 5601–5603.
[43] X.H. Huang, Z.Y. Zhan, K.P. Pramoda, C. Zhang, L.X. Zheng, S.J. Chua, J. Cryst. Eng. Commun. 14 (2012) 5163–5165.
[44] A.R. Reichle, K.G. McCurdy, L.G. Hepler, Can. J. Chem. 53 (1975) 3841–3845.
[45] W.J. Li, E.W. Shi, W.Z. Zhong, Z.W. Yin, J. Cryst. Growth 203 (1999) 186–196.
[46] K. Biswas, B. Das, C.N.R. Rao, J. Phys. Chem. C 112 (2008) 2404–2411.
[47] S.M. Lam, J.C. Sin, A.Z. Abdullah, A.R. Mohamed, Desalin. Water Treat. 41 (2012) 131–169.
[48] A. Mclaren, T.V. Solis, G. Li, G. Li, S.K. Tsang, J. Am. Chem. Soc. 131 (2009) 12540–12541.
[49] M.Y. Guo, A.M.C. Ng, F.Z. Liu, A.B. Djurisic, W.K. Chan, H.M. Su, K.S. Wong, J. Phys. Chem. C 115 (2011) 11095–11101.
[50] H.F. Zhai, A.D. Li, J.Z. Kong, X.F. Li, J. Zhao, B.L. Guo, J. Yin, Z.S. Li, D. Wu, J. Solid State Chem. 202 (2013) 6–14.